Atom-projected and angular momentum resolved density of states in the ONETEP code

Electronic Structure

OPEN ACCESS

PAPER

Atom-projected and angular momentum resolved density of states in the ONETEP code

J Aarons[1,3], L G Verga[2,3], N D M Hine[1] and C-K Skylaris[2]

[1] Department of Physics, University of Warwick, Coventry, CV4 7AL, United Kingdom
[2] School of Chemistry, University of Southampton, Highfield, Southampton SO17 1BJ, United Kingdom
[3] Both authors contributed equally to this manuscript.

E-mail: c.skylaris@soton.ac.uk

RECEIVED
21 May 2019

REVISED
4 July 2019

ACCEPTED FOR PUBLICATION
22 July 2019

PUBLISHED
21 August 2019

Keywords: density of states, projected density of states, linear scaling DFT, large scale DFT, local density of states

Supplementary material for this article is available online

Abstract

Local and angular momentum projected densities of states (DOS) are invaluable sources of information that can be obtained from density functional theory calculations. In this work, we describe a theoretical framework within ONETEP's linear-scaling DFT formalism that allows the calculation of local (atom-projected) and angular momentum projected density of states l-p-DOS. We describe four different bases that can be used for projecting the DOS with angular momentum resolution and perform a set of tests to compare them. We validate the results obtained with ONETEP's l-p-DOS against the plane-wave DFT code CASTEP. Comparable results between ONETEP's and CASTEP's charge spilling parameters are observed when we use pseudo-atomic orbitals as the projection basis sets. In general, the charge spilling parameters show remarkably low values for projections using non-contracted spherical waves as the angular momentum resolved basis. We also calculate the *d*-band and *d*-band centres for Pt atoms in (1 1 1) facets of cuboctahedral Pt nanoparticles of increasing size, which is an example of l-p-DOS application commonly used as an electronic descriptor in heterogeneous catalysis. Interestingly, the different projection bases lead to similar conclusions, showing the reliability of the implemented method for such studies. The implementation of these methods in a linear-scaling framework such as ONETEP provides another tool for analysing the electronic structure of complex nanostructured materials.

1. Introduction

It is now well-established that density functional theory (DFT) calculations play an important role in scientific development, with an impact described in detail in several recent review papers [1–3], and confirmed by the evolution of citations of the papers containing DFT's theoretical foundations [4, 5]. The applicability of DFT to so many diverse areas has motivated the development of many different formalisms and implementations of DFT to provide users with computationally efficient codes for different systems.

One of the most significant considerations guiding the choice of an appropriate DFT code for the study of a specific system is the basis set used to represent the single particle wave functions. Atomic-like orbitals are a common choice, but in many cases, using a variety of other forms of function can be more computationally efficient or accurate. A good example is the widely used plane wave DFT formalism, where the basis set that can be improved systematically, being extremely efficient to deal with periodic and extended systems.

However, atom-like basis sets are still necessary to calculate certain properties of the electronic structure, and projection schemes are often required to allow the calculation of the desired quantity. Pioneering work by Sanchez-Portal [6, 7] showed how the eigenfunctions obtained with a plane wave DFT code were projected onto localised atomic-like-orbitals, which allowed local quantities such as atomic charges or local density of states to be computed. In addition to built-in functionality in many plane-wave DFT codes, projection schemes and localised property calculations can also be found in post-processing codes, such as LOBSTER [8], which uses projection to compute several local properties.

In particular, the local (atom projected) density of states (l-DOS) and the angular momentum projected density of states (p-DOS) are useful tools to obtain information and insight relevant to important applications. For example, in the field of heterogeneous catalysis, the density of states projected onto the *d*-band at metallic surfaces is a powerful descriptor of a surface's bonding ability, which can be used to estimate its efficiency as a catalyst for a given reaction.

Computational catalysis researchers have found scaling relations between adsorption energies of different adsorbates on metallic surfaces and scaling relations between adsorption energies and reaction barriers that lead to the so-called volcano plots of activity [9]. These volcano plots show that an optimum catalyst should have a 'bonding strength' to atoms and molecules involved in the reaction that enables the reactants to bind to the surface and be activated, but that does not hinder the desorption of the products [10, 11]. Concurrently, the *d*-band model [12] shows a correlation between adsorption energies strengths and some properties of the *d*-band of a metallic surface, such as its centre [13], width [14], and upper edge [15]. These findings allow using information from the *d*-projected density of states as indications about how a metallic surface would behave as a catalyst. Such structure-property relationships are pivotal for rational catalyst design, showing the importance of l-p-DOS calculations for this research field.

Our focus in this paper is the ONETEP linear-scaling DFT package, which has recently been used for applications that benefit from l-p-DOS calculations, including studies with metallic nanoparticles applied to heterogeneous catalysis [16–19]. In the ONETEP linear scaling DFT formulation, the density matrix is represented via non-orthogonal generalised Wannier functions (NGWFs) that are optimised *in situ*. These atom-centered NGWFs have previously been used to define a l-DOS scheme [20] which has found widespread use. However, after optimisation, the NGWFs are no longer pure in terms of their angular momentum decomposition. Thus, it is necessary to develop and apply a projection scheme to obtain angular momentum resolved properties. Here, we discuss the ONETEP formalism, our choices for the angular momentum resolved basis set, and the implementation of the l-p-DOS method in the ONETEP code. We present test cases, comparing different angular momentum resolved basis sets used to construct the l-p-DOS and comparing the results obtained with ONETEP to similar calculations performed with the CASTEP plane-wave code [21].

2. The ONETEP code

ONETEP (Order-N electronic total energy package) [22] is a DFT package designed to scale linearly with the number of atoms in the system while retaining some advantages of plane-wave approaches, such as a systematic means to improve the accuracy of the underlying basis. In ONETEP the density matrix is constructed as

$$\rho(\vec{r},\vec{r}') = \sum_{\alpha\beta} \phi_\alpha(\vec{r}) K^{\alpha\beta} \phi^*{}_\beta(\vec{r}') \tag{1}$$

where ϕ are the localised non-orthogonal generalised Wannier functions (NGWFs) and $K^{\alpha\beta}$ is the density kernel matrix. The Kohn–Sham orbitals are related to the NGWFs by

$$|\psi_i\rangle = |\phi_\alpha\rangle M_i^\alpha \tag{2}$$

where M_i^α are the expansion coefficients for the ϕ_α NGWFs.

The NGWFs are themselves expanded in terms of a basis of psinc functions [23] which are distributed over the points of a regular grid in real-space whose spacing is controlled by a single parameter. The energy minimisation in ONETEP is performed in two nested loops, one that optimises the density kernel for a fixed set of NGWFs and the other that optimises the NGWFs *in situ*, allowing the control of the basis set accuracy with a minimal number of NGWFs.

In addition to the locality imposed to the NGWFs, ONETEP also exploits the concept of electronic matter nearsightedness [24] to control the sparsity of the density kernel matrix and pursue linear-scaling computational cost.

3. Projected density of states in ONETEP

The density of states (DOS) is a function of the energy (ϵ) that can be defined as:

$$\rho(\varepsilon) = \sum_i \langle\psi_i|\psi_i\rangle \delta(\varepsilon - \varepsilon_i). \tag{3}$$

Using the relation from equation (2), we can express this in terms of NGWFs as

$$\rho(\varepsilon) = \sum_i M_i^{\dagger\alpha} \langle\phi_\alpha|\phi_\beta\rangle M^\beta{}_i \delta(\varepsilon - \varepsilon_i). \tag{4}$$

To construct an angular momentum projected density of states from ONETEP's NGWFs, we first need to define an angular momentum resolved basis, project the eigenfunctions obtained with the NGWFs to this representation and construct a weights matrix that allows summation over particular angular momentum and atoms to decompose the total DOS function. In the following sections, we show the possible choices of angular momentum resolved basis and the methodology used to construct l-p-DOS implemented in ONETEP.

3.1. Choice of angular momentum resolved basis

The angular momentum resolved basis functions all have the form of a spherical harmonic, $Z_{l,m}(\Omega)$ multiplied by a radial part, where Ω stands for the angular dependence (solid angle). The form of the radial part is where we have some flexibility. Provided that we choose functions which capture enough of the character of the NGWF representation, resulting in a small spilling parameter and a small number of basis functions in the set, the set will be considered adequate. The definition of a 'small' spilling parameter and the number of basis functions considered to be to many or too few is arbitrary and will be explored from now on.

We have explored four options of angular momentum resolved basis, where three of them are based on spherical waves (SW) basis sets. We have as options a non-contracted, full set of SWs; a contracted set with unity contraction weights (C-SWs), a contracted set with contraction weights defined through an inner product with each NGWF, our so-called fitted set (CF-SWs); and finally a set of pseudo-atomic orbitals (PAOs) which is the only set not based directly on SWs, although ultimately the PAOs are themselves expressed via coefficients multiplying the full set of SWs. The pseudo-atomic orbitals are already in use within ONETEP as an starting point from which the NGWFs are optimised, so may represent a low spilling option for the projection of the NGWFs.

We choose the spherical wave (SW) basis as an option so that we can tune the size of the basis systematically to reduce the amount of spilling to the appropriate levels for the application of each calculation. As listed before, this leaves us with some choice, however, in how (or if) we choose to contract the basis functions. Contraction is desirable mainly because our SW basis is not only resolved in the azimuthal quantum number, l, giving the desired angular momentum resolution, but also in magnetic quantum number m and implicitly in the principal quantum number, through the bessel functions, j_l. The number of basis functions in this set may be prohibitive for practical calculations, so we can contract over m and j_l.

The spherical waves are generated on the same equispaced grid as we use for NGWFs and are defined as:

$$\chi_{Ak_{nl}lm}(\vec{r}) = j_l(k_{nl}r)Z_{lm}(\Omega)H(a-r), \tag{5}$$

where A represents an atom, H is a Heaviside step function which cuts off any contribution to the spherical waves outside of a radius, a, and $\vec{r}$ is the vector from the nucleus of the corresponding atom. For each SW, k_{nl} is chosen such that $k_{nl}\,a$ is the nth zero of the spherical Bessel function $j_l(x)$.

Contracted spherical waves (C-SWs) are defined in terms of these SWs as:

$$\chi_{Alm}(\vec{r}) = \sum_{k_{nl}} \omega_{Ak_{nl}lm}\chi_{Ak_{nl}lm}(\vec{r}), \tag{6}$$

where $\omega_{Ak_{nl}lm}$ are the contraction coefficients. For the set denoted C-SWs these are set to 1.

The contraction coefficients can also be set to fit the NGWFs, generating a set of angular momentum resolved functions that we call contracted and fitted spherical waves (CF-SWs). However, in the case that we fit to the NGWFs, we instead take a set of l and m CF-SWs on every NGWF of every atom, rather than one set per atom. This typically increases the size of the spherical wave basis by a factor of 4 for elements up to (and including) the third row of the periodic table and by a factor of 13 for the first transition series, and so on for heavier elements. In this case, the CF-SWs are defined as:

$$\chi_{\alpha lm}(\vec{r}) = \sum_{k_{nl}} \omega_{\alpha k_{nl}lm}\chi_{Ak_{nl}lm}(\vec{r}), \tag{7}$$

where contraction coefficients $\omega_{\alpha k_{nl}lm}$ which best fit the NGWF ϕ_α can be calculated by taking the inner product of each NGWF with each SW on the same center:

$$\omega_{\alpha k_{nl}lm} = \langle \phi_\alpha | \chi_{Ak_{nl}lm} \rangle. \tag{8}$$

It is possible in this approach that contraction coefficients on an NGWF sum to zero, which will lead to a non-positive definite overlap matrix, if left untreated. One approach to overcome this problem would be to remove this CF-SW from the set, but instead we opt to leave it in place, recording its index and dealing with it in the resolution of identity, as we explain in the next section.

Another option that we have is to use pseudoatomic orbitals (PAOs) as our angular momentum resolved basis. PAOs are solutions to the atomic Kohn–Sham equation and have the form:

$$\varphi_n(\mathbf{r}) = \sum_{\nu} c_{n,\nu} B_{l_n,\nu}(r) Z_{l_n m_n}(\Omega), \tag{9}$$

where $B_{l_n,\nu}(r)$ are normalised spherical Bessel functions and $c_{n,\nu}$ are a set of coefficients obtained by solving the Kohn–Sham equation for each atom species with spherical localisation constraints using the same cutoff radius as the one used for the NGWFs. Since the PAOs are used for the initialisation of NGWFs [25], to also use them as the angular momentum resolved basis requires no extra calculations associated with the generation of the set. The number of PAOs per atom, N, is the same as the number of NGWFs, typically a number associated with subshell-filling (i.e. 1,4,9,13,...).

3.2. Resolution of identity and construction of the projected DOS

Once we have chosen and constructed an angular momentum resolved basis set, we can then construct an identity operator. This can be expressed in terms of the basis functions and their inverse overlap matrix $\Lambda^{\alpha lm,\beta l'm'}$ as:

$$\hat{1} = |\chi'_{\alpha lm}\rangle \Lambda^{\alpha lm,\beta l'm'} \langle \chi'_{\beta l'm'}|. \tag{10}$$

A 'good' angular momentum resolved basis set $\chi'_{\alpha lm}$ for a given set of NGWFs is implicitly defined by the requirement that

$$\langle \phi_\alpha | \hat{1} | \phi_\beta \rangle \approx \langle \phi_\alpha | \phi_\beta \rangle \,, \tag{11}$$

in which case it will be safe to insert this resolution of the identity into the density of states from equation (4) without incurring significant 'spillage'. We thus obtain:

$$\rho(\varepsilon) \approx \sum_i M_i^{\dagger\alpha} \langle \phi_\alpha | \chi'_{\alpha lm} \rangle \Lambda^{\alpha lm,\beta l'm'} \langle \chi'_{\beta l'm'} | \phi_\beta \rangle M^\beta{}_i \, \delta(\varepsilon - \varepsilon_i). \tag{12}$$

The major advantage of defining the DOS in terms of this identity operator is that it allows us to exploit the angular momentum dependence of $|\chi_{\alpha lm}\rangle$, by selectively summing over particular angular momentum components l and m to create the angular momentum projected DOS.

To calculate the angular momentum projected density of states, we firstly rewrite equation (12) in terms of a weights matrix, $W_{\alpha lm,i}$:

$$\rho(\varepsilon) = \sum_{\alpha,l,m,i} W_{\alpha lm,i} \delta(\varepsilon - \varepsilon_i), \tag{13}$$

where $W_{\alpha lm,i}$ is defined to be the Hadamard product of two matrices defined as a left and a right part of the identity matrix expression in equation (12), such that

$$W_{\alpha lm,i} = R^{\alpha lm}{}_i \circ T_{\alpha lm,i} \tag{14}$$

and under the condition that

$$\sum_{\alpha lm} W_{\alpha lm,i} = M_i^{\dagger\alpha} \langle \phi_\alpha | \chi'_{\alpha lm} \rangle \Lambda^{\alpha lm,\beta l'm'} \langle \chi'_{\beta l'm'} | \phi_\beta \rangle M^\beta{}_i. \tag{15}$$

The effect of this is to change the order of operations with respect to equation (12), so that instead of producing an element in the identity matrix by multiplying each element of a row in the $\mathbf{R}^T$ matrix by each element of a column in the $\mathbf{T}$ matrix and summing all products in the row and column pair, we instead construct an element in the $\mathbf{W}$ matrix by taking the elementwise product of $\mathbf{R}$ and $\mathbf{T}$ and summing over the elements in the columns of $\mathbf{W}$. This allows for the final sums to be taken over restricted sets of indices, as we require.

For instance, the angular momentum projected density of states can be written as

$$\rho_l(\varepsilon) = \sum_{\alpha m,i} W_{\alpha lm,i} \delta(\varepsilon - \varepsilon_i), \tag{16}$$

or the local angular momentum projected density of states can be written as

$$\rho_{\mathscr{S},l}(\varepsilon) = \sum_{\alpha(\mathscr{S}),m,i} W_{\alpha lm,i} \delta(\varepsilon - \varepsilon_i), \tag{17}$$

where $\alpha(\mathscr{S})$ means the subset of α associated with the set of atoms, $\mathscr{S}$.

Finally, we note that the $R^{\alpha lm}{}_i$ and $T_{\alpha lm,i}$ matrices can be defined in many ways. In our implementation, we choose to define the matrices using a symmetric decomposition achieved by taking the Löwdin decomposition of $\Lambda^{\alpha lm,\beta l'm'}$, which can be expressed in terms of its eigenpairs,

$$\mathbf{\Lambda Q} = \lambda \mathbf{Q}, \tag{18}$$

as:

$$\mathbf{\Lambda}^{\frac{1}{2}} = \mathbf{Q} \lambda^{\frac{1}{2}} \mathbf{Q}^T, \tag{19}$$

where $\mathbf{Q}$ is the matrix of eigenvectors of $\mathbf{\Lambda}$ and $\lambda^{\frac{1}{2}}$ is the diagonal matrix of square-rooted eigenvalues of $\mathbf{\Lambda}$.

The $\mathbf{T}$ matrix in the symmetric decomposition may then be expressed as

$$T_{\alpha lm,i} = \left(\mathbf{\Lambda}^{\frac{1}{2}}\right)_{\alpha lm}^{\ \ \beta l'm'} \langle \chi'_{\beta l'm'} | \phi_\beta \rangle M^{\beta}_{\ i}, \tag{20}$$

where $T_{\alpha lm,i}$ has invariant indices in this case, and $W_{\alpha lm,i}$ from equation (14) can be defined as its elementwise square

$$W_{\alpha lm,i} = T^2_{\alpha lm,i}. \tag{21}$$

For all the implemented angular momentum resolved basis, we can define the spilling parameter s, as

$$s = \frac{1}{N_{\mathrm{MO}}} \sum_{i}^{N_{\mathrm{MO}}} \left\{ 1 - \sum_{\alpha lm} W_{\alpha lm,i} \right\}, \tag{22}$$

this helps to quantify how good the angular momentum projected basis is in terms of the accuracy of the identity operator. We will use the spilling parameter later in the paper to assess the quality of our sets.

The problem of having basis functions with zero weight leading to eigenvalues of zeros in the C-SWs overlap matrix, discussed in section 3.1 may be dealt with by not inverting $\Lambda_{\alpha lm,\beta l'm'}$ to form $\Lambda^{\alpha lm,\beta l'm'}$ or $\left(\mathbf{\Lambda}^{-\frac{1}{2}}\right)^{\alpha lm,\beta l'm'}$, but instead by taking its eigenvalue decomposition

$$\mathbf{\Lambda}^{-\frac{1}{2}} = \mathbf{Q} f(\lambda) \mathbf{Q}^T, \qquad f(\lambda) = \begin{cases} 0 & \lambda < 0 \\ \lambda^{-\frac{1}{2}} & \lambda >= 0 \end{cases}, \tag{23}$$

which is equivalent to dropping basis functions which lead to non-positive definite overlap matrices. This operation requires a diagonalisation, however, if we need to avoid this, we will need to drop basis functions with zero weights and to use an iterative inversion or Löwdin algorithm.

The projected weights allows us to construct various types of DOS. For example, to construct the DOS for the p electrons of a subset of atoms, we can add up all the weights for $l' = 1$ and restrict the summation to the selected atoms:

$$\rho_{p,\mathscr{S}}(\varepsilon) = \sum_{\alpha \in \mathscr{S}, m', i} W_{\alpha 1 m', i} \delta(\varepsilon - \varepsilon_i). \tag{24}$$

This expression was derived for the case of norm-conserving pseudopotentials where ψ_i are the pseudo wavefunctions. In the case of PAW calculations, equation (3) becomes

$$\rho(\epsilon) = \sum_i \langle \tilde{\psi}_i | \hat{S} | \tilde{\psi}_i \rangle \delta(\varepsilon - \varepsilon_i), \tag{25}$$

where $\hat{S}$ is the PAW overlap operator defined in terms of the PAW transformation operator $\hat{\tau}$ between pseudo and all-electron wavefunctions as $\hat{S} = \hat{\tau}^\dagger \hat{\tau}$, and $\tilde{\psi}_i$ are the smooth valence wavefunctions.

4. Calculation details

We performed our simulations with the ONETEP code [22] and with CASTEP [21] as a reference code to validate our implementation. For metallic systems in ONETEP, we used the ensemble DFT method, as implemented by Serrano and Skylaris [26]. For all calculations, we adopted PBE [27] as our exchange-correlation functional. The ONETEP calculations were conducted using the projector augmented wave (PAW) method [28], as implemented in ONETEP by Hine [29], while in CASTEP the calculations were conducted with ultrasoft pseudopotentials [30]. For all the calculations, we have used the GBRV library for ultrasoft and PAW potentials [31]. We have used the OptaDOS [32] code to post-process the results from CASTEP calculations and obtain the l-p-DOS data and set the mid-gap level from ONETEP calculations as zero for all l-p-DOS plots.

In ONETEP, we set the psinc basis set [23] kinetic energy cutoff to 550 eV for geometry optimisations and 850 eV for properties calculations, with the NGWFs radii set to 9.0 a_0, which has been previously shown to give good convergence for these systems [16–19, 33]. For CASTEP, the kinetic energy cutoff was equal to 450 eV. We performed our simulations under periodic boundary conditions, with a minimum vacuum gap of 10 Å between the borders of the simulation box and any simulated atom. The somewhat lower kinetic energy cutoff required in CASTEP for good convergence compared to ONETEP is largely the result of the need, in ONETEP, for a good description of the discontinuity at the edge of NGWFs spheres. Note also that there is not a direct correspondence between equivalent cutoff values in CASTEP and ONETEP, because the plane-wave basis in CASTEP includes a sphere of G-vectors up to a cutoff defined by $\frac{1}{2}|\vec{G}|^2 < E_{\mathrm{cut}}$, whereas ONETEP uses a real-space grid with a cutoff defined by the same criterion, so implicitly the whole box of G-vectors is used as the basis.

Table 1. Charge spilling parameter, presented as percentages, for calculations performed with CASTEP, which uses its own set of PAOs as the basis set for of its charge spilling calculations, and different angular momentum resolved bases in ONETEP.

System	SWs (%)	C-SWs (%)	CF-SWs (%)	PAOs (%)	CASTEP (%)
CO	0.19	26.78	6.45	1.59	1.66
C_2H_2	0.04	17.92	16.47	1.77	1.89
C_2H_4	0.03	13.55	7.44	1.83	1.91
C_2H_6	0.02	11.02	6.96	1.70	1.78
SiH_4	0.08	11.82	10.11	2.40	2.79
$LiPF_6$	0.30	17.62	7.87	0.94	0.90
Pd_{13}	0.00	19.73	0.28	0.08	0.10
Pt_{13}	0.01	22.70	0.41	0.06	0.13
Pt_{55}	0.01	19.28	0.17	0.07	0.11
Pt_{147}	0.00	17.83	0.01	0.07	0.10
Pt(1 1 1)	0.00	15.75	0.05	0.06	0.08

The structures used to compute the projected density of states were optimised in ONETEP [34], where the geometries were relaxed with a convergence threshold of 0.002 Eh/a_0 on the atomic forces. The only exceptions are the Pt slabs and nanoparticles. For these cases, the structures were constructed with bond lengths from the optimised Pt bulk geometry. For all the calculations, the SWs, C-SWs, and CF-SWs were created using a total of 16 functions per magnetic quantum number m per atom.

5. Demonstration of the method

The spilling parameter presented in equation (22) measures the ability of the basis set to represent the whole manifold of calculated states. Since we aim to compare our basis sets against the equivalent spilling parameter calculated within plane wave methods such as CASTEP, we require a further modification, since plane-wave methods generally restrict the spilling parameter calculation to the occupied bands [7]. A general form of the charge spilling parameter able to deal with fractional occupancies can be written as:

$$s_q = 1 - \left\{ \frac{\sum_i \sum_{\alpha lm} f_i W_{\alpha lm,i}}{\sum_i f_i} \right\}, \tag{26}$$

where f_i are the occupancies and $W_{\alpha lm,i}$ the weights matrix as defined in equation (15).

To compare the quality of the angular momentum resolved bases, we present in table 1 the charge spilling parameter for different systems. We calculated the l-p-DOS for a CO molecule, a set of hydrocarbons, a silane molecule, a $LiPF_6$ compound in the C_{4v} symmetry, a set of cuboctahedral metallic nanoparticles (Pt and Pd) and a platinum slab with 320 atoms and a (1 1 1) facet exposed. We performed the calculations using all the available l-p-DOS bases in ONETEP, namely: (i) non-contracted spherical waves (SWs); (ii) contracted spherical waves (C-SWs); (iii) contracted spherical waves with coefficients fitted to the NGWFs (CF-SWs) and; (iv) pseudo-atomic orbitals (PAOs).

Table 1 shows a general trend in the charge spilling parameters, namely that SWs $<$ PAOs $\leqslant$ CASTEP PAOs $<$ CF-SWs $<$ C-SWs. The small values obtained with SWs were expected due to the large size and flexibility of the basis. The results obtained with PAOs in ONETEP and CASTEP indicate that the implementation in both codes is comparable and that we should also expect similar results for pDOS calculations. We can also note that the spilling parameters from CASTEP are slightly higher than the ones obtained with PAOs in ONETEP, which can be seen as a consequence of the localisation of the NGWFs in spheres with the same radius as the PAOs, whereas in CASTEP the wavefunctions are delocalised over the simulation box. Table 1 also shows that determining the contraction coefficients by fitting the C-SWs to the NGWFs contributes to reducing the spilling parameter as compared with contraction of spherical waves using unit weights. For the calculations with metallic nanoparticles, all the pDOS options, with the exception of C-SWs, show similar values of spilling parameters, indicating that the projected density of states obtained with these approaches should also be comparable to each other.

We compare in figure 1 projected density of states obtained with CASTEP and the ones obtained with PAOs in ONETEP. Figures 1(a) and (b) show, respectively, the density of states projected onto s and p orbitals for a C_2H_4 molecule. Figure 1(c) tests, simultaneously, the local and angular momentum projected density of states, by showing the DOS projected onto the d-channel only for Pt atoms in a (1 1 1) facet of a cuboctahedral Pt_{13} nanoparticle.

In accordance with the results obtained for the charge spilling parameters, here we see a very high degree of agreement between ONETEP and CASTEP results. This is also observed for several other tested systems but omit-

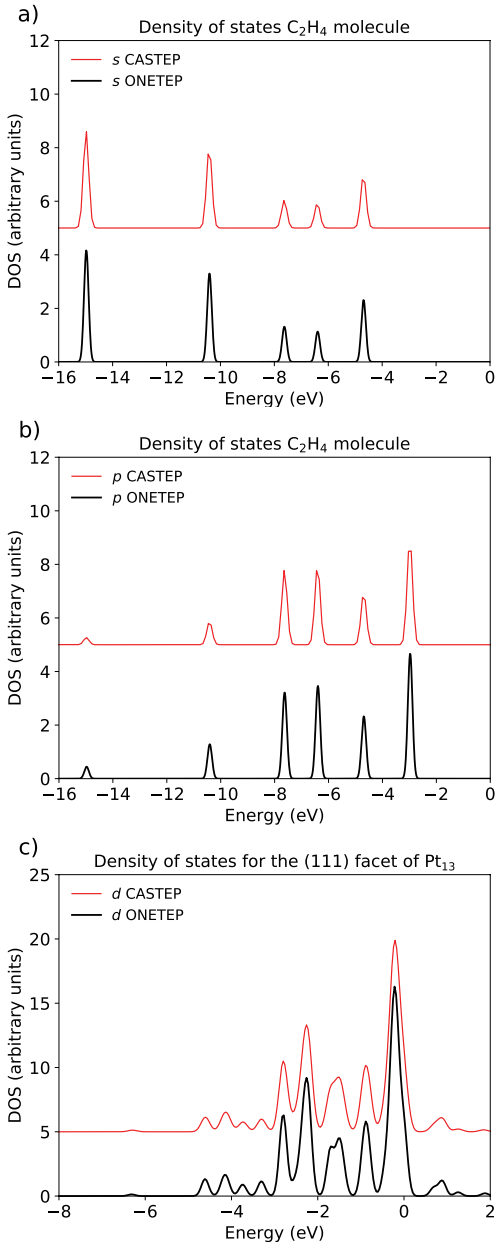

Figure 1. Comparison between ONETEP and CASTEP projected density of states using PAOs as the angular momentum resolved basis. (a) and (b) Show, respectively, the density of states resolved as *s* and *p* contributions for a C_2H_4 molecule. (c) shows the *d*-channel of Pt atoms in a (1 1 1) facet of a cuboctahedral Pt_{13} nanoparticle. CASTEP results are offset vertically for comparison.

ted here for conciseness but detailed in the supplementary information (stacks.iop.org/EST/1/035002/mmedia). The pDOS similarity in both codes validates the implementation of the projected density of states in ONETEP. From now on, we will use only the results obtained with the PAOs in ONETEP to compare with other basis sets.

Figure 2 compares all the implemented angular momentum resolved basis sets, testing the results for CO, C_2H_4 and C_2H_6. Figures 2(a), (c) and (e) show, respectively, the density of states of CO, C_2H_4 and C_2H_6 projected onto *s* channels, while (b), (d) and (f) shows the projections for *p* channels of the same molecules. In general, the projections with all the angular momentum resolved bases are similar. The generation of the non-contracted spherical waves set is unbiased and, as demonstrated with the charge spilling parameters, provides an almost complete projection of the calculated bands for a wide range of systems. In this sense, the similarity of the pDOS obtained with PAOs and non-contracted SWs reinforces the idea that PAOs are viable options to obtain angular momentum projected density of states.

The main differences arise when calculating systems with atoms with valence shells composed by different values of azimuthal quantum numbers. The spherical wave basis is constructed with the same maximum *l* for every atom in the whole system. For example, for a hydrocarbon, the SWs are constructed with s and p functions for carbon and hydrogen atoms. Meanwhile, the PAOs are constructed by default in ONETEP as a minimum

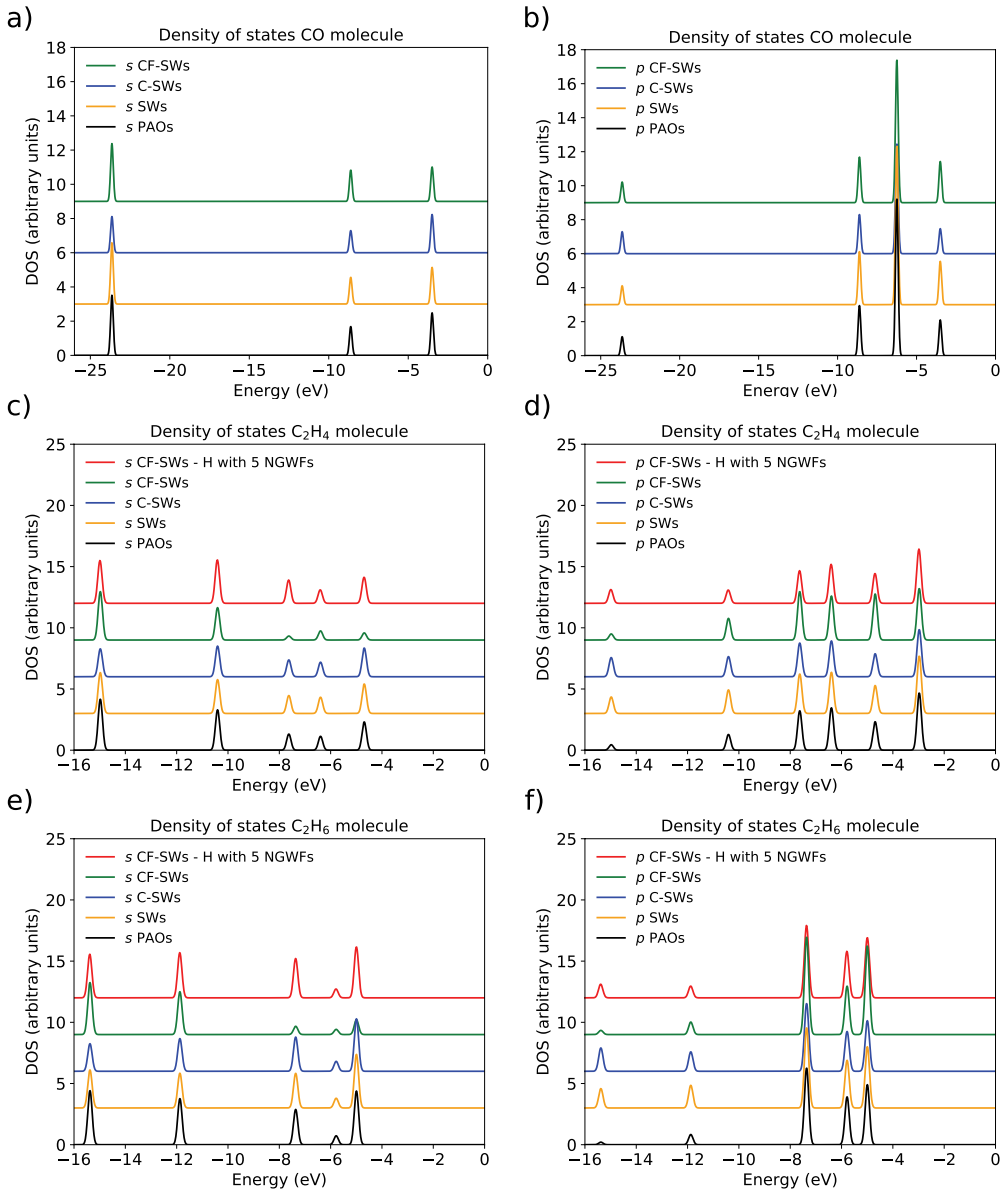

Figure 2. Projected density of states (p-DOS) for different schemes implemented in ONETEP. (a), (c) and (e) show, respectively, *s* p-DOS for CO, C_2H_4, and C_2H_6. (b), (d) and (f) show the *p* projection for the same molecules. For all plots, different colors are used to represent each bases, where black, orange, blue and green represent PAOs, SWs, C-SWs and CF-SWs. For (c)–(f) the CF-SWs calculated with 5 NGWFs for each hydrogen atom are represented in red.

basis set to initialise the NGWFs, which results on basis with *s* and *p* character for carbon atoms and only *s* character for hydrogen, generating small variations in the pDOS peaks as compared to SWs.

For example, in the carbon monoxide tests in figures 2(a) and (b), both oxygen and carbon atoms have *s* and *p* orbitals and the computed pDOS for all approaches is almost identical. Meanwhile, for C_2H_4 and C_2H_6, some variations are observed depending on the chosen basis set, where the projections performed with non-contracted spherical wave basis show more *p* character as compared to the PAO basis for the lowest energy peaks on both hydrocarbons.

Out of all the contracted spherical wave schemes, the CF-SWs is the one that presents largest variations from PAOs and non-contracted SWs. We attribute this to the difficulty of fitting a spherical wave basis composed of s and p functions to a single NGWF. Thus, we have tested the effect of including five NGWFs on hydrogen atoms, so as to initialise them with *s* (2 NGWFs) and *p* (3 NGWFs) character. As a result, the calculated charge spilling parameters decrease from 7.44% to 3.69% for C_2H_4 and from 6.96% to 2.33% for C_2H_6, and the overall behaviour observed with non-contracted spherical waves is recovered.

As briefly discussed in the introduction, angular momentum projected density of states is an invaluable tool for theoretical investigations in the field of heterogeneous catalysis. In this area, describing the interaction between the catalyst surface and adsorbates is essential to explain and predict catalytic activities. As proposed by Nørskov *et al* [12, 13], properties of the localised *d*-band of transition metals can be used as electronic descriptors

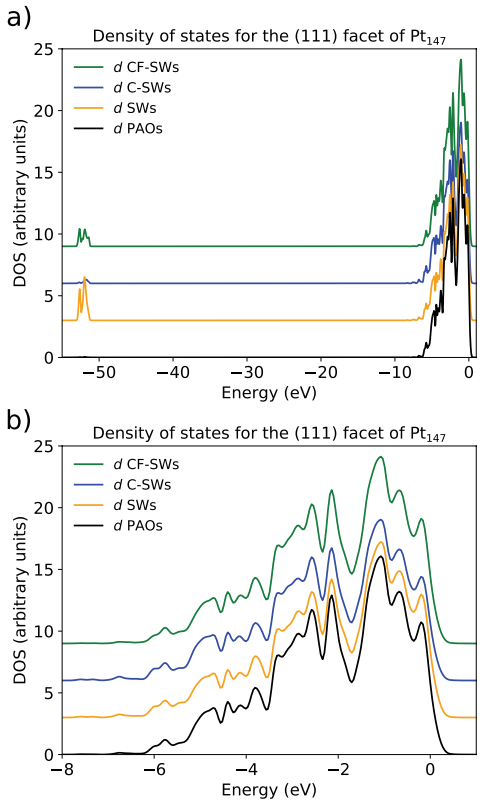

Figure 3. Density of states projected onto the *d* channels of Pt atoms in a (1 1 1) facet of a Pt_{147} nanoparticle where (a) spans over the full range of calculated energy levels whereas (b) focusses on the states near the Fermi level. For both plots, black, yellow, blue and green lines represent densities of states obtained with PAOs, SWs, C-SWs and CF-SWs.

of the interaction strength between and adsorbate and the catalyst surface. Specifically, as there is a connection between the *d*-band centre and the surface composition, crystallographic orientation, site coordination and nanoparticle sizes, studies with such descriptors can be used to search for directions to catalysts optimisations.

Here, to test the suitability of our l-p-DOS methods for application to this area, we have decided to compute cuboctahedral platinum nanoparticles of increasing size, ranging from Pt_{13} to Pt_{561} and a Pt slab with a (1 1 1) facet exposed. We have also computed a Pd_{13} cluster as an additional test. Increasing the nanoparticle size affects the Pt–Pt bond lengths at the surface, and the ratio between uncoordinated and coordinate sites. This generates shifts in the *d*-band centres that translate into a weakening in the interaction with adsorbates. Here, we are not considering the changes in the Pt–Pt bond lengths with increasing nanoparticle sizes. We compute Pt nanoparticles created with Pt bulk bond lengths to isolate the electronic effects to the geometrical changes due to size effects.

Figures 3(a) and (b) present the density of states projected onto the *d* channels of Pt atoms in a (1 1 1) facet of a Pt_{147} nanoparticle. The first plot spans all the calculated energy levels and the second focuses on the states near the Fermi level. These plots show that *d*-bands calculated with all the implemented basis sets are similar. The overall shape of the *d*-band near the Fermi level remains almost unchanged for all basis sets, with only small variations in terms of peak intensities. The main differences appear for low energy levels, where additional *d*-projected states are observed for spherical wave based approaches. In practice, as the energy levels near the Fermi level are the important region for catalysis applications, and these results are similar for all basis set options, these differences should not affect the overall applicability of any of the schemes.

Figure 4(a) shows the *d*-band centres calculated with different approaches for the (1 1 1) facet of the nanoparticles against the nanoparticles sizes. The *d*-band centres are calculated using the occupancy-weighted l-p-DOS and focusing on the states near the Fermi-level, i.e. excluding the variations for low energy levels commented on figure 3. As we increase the nanoparticle size, the *d*-band centre moves away from the Fermi-level, which according to the *d*-band theory should describe a weaker interaction with adsorbates.

Figure 4(b) shows how the calculated *d*-band centres with spherical waves bases (SWs, C-SWs, CF-SWs) compare to the same quantities calculated using PAOs. We show the *d*-band centres for the whole (1 1 1) facet of Pt nanoparticles of increasing size, the exposed facet of the Pt (1 1 1) slab and the (1 1 1) facet of Pd_{13}. As observed, the small changes in the projected density of states plots are not crucial for the calculated *d*-band centres and similar trends and conclusions for the catalytic activity of the nanoparticles could be obtained with any method.

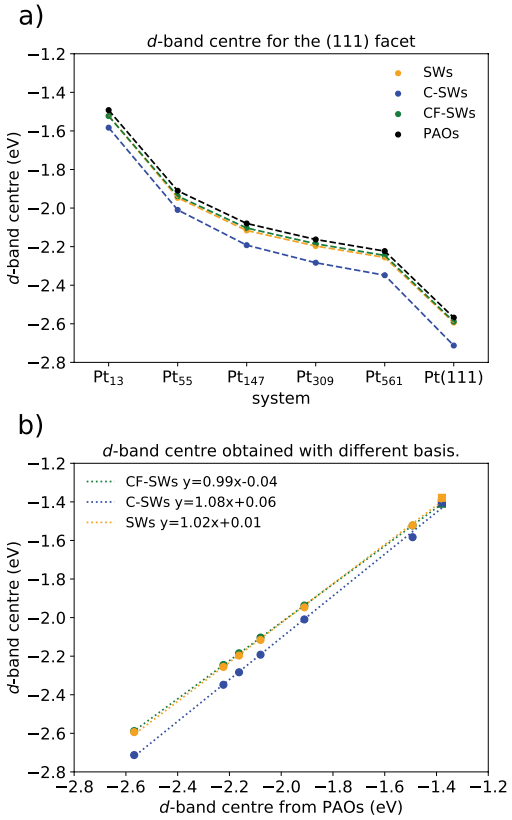

Figure 4. Calculated *d*-band centres using different projection schemes. (a) Shows the results for (1 1 1) facets of Pt nanoparticles against the nanoparticles sizes and for a Pt(1 1 1) slab. (b) Compares the calculated *d*-band centres with spherical waves bases (SWs, C-SWs, CF-SWs) to the same quantities obtained using PAOs, showing the *d*-band centres for the whole (1 1 1) facet of Pt nanoparticles of increasing size, the exposed facet of the Pt (1 1 1) slab, and the (1 1 1) facet of Pd_{13} (square symbols). The *d*-band centres are calculated using the occupancy-weighted l-p-DOS and focusing on the states near the Fermi-level to exclude the variations for the low energy levels illustrated in figure 3. For all plots, different colors are used to represent each bases, where black, yellow, blue and green represent PAOs, SWs, C-SWs and CF-SWs.

6. Conclusions

In this work, we have described the underlying theoretical framework for the implementation of angular momentum projected density of states within the ONETEP formalism. We presented four options of angular momentum resolved basis sets that were implemented in ONETEP to obtain l-p-DOS. The first three are based on spherical waves, with a non-contracted set of SWs; a contracted set with unity contraction weights (C-SWs), and a contracted set where the contraction weights are determined via inner products with the NGWFs (CF-SWs). Pseudo-atomic orbitals (PAOs) are used for the fourth basis set, which is also the initialisation of NGWFs in ONETEP.

We performed tests on several systems to assess how the projection varies with changes in the basis sets and how the ONETEP's results compare to l-p-DOS functionality in CASTEP. We have calculated the density of states for a CO and a silane molecule, a set of hydrocarbons, a $LiPF_6$ compound, metallic nanoparticles of different sizes, and one platinum slab with 320 Pt atoms. In terms of charge spilling parameter, we observed a similar trend for all tested systems, with SWs $<$ PAOs $\leqslant$ CASTEP $<$ CF-SWs $<$ C-SWs. For the non-contracted SWs basis, small charge spilling parameters $s_q < 1\%$ were observed for all systems. For PAOs, the charge spilling parameters obtained with ONETEP and CASTEP were almost identical, and for contracted SWs basis, the option with contraction weights obtained by fitting the NGWFs presented lower s_q values than the one with unit contraction weights.

Despite some differences in the charge-spilling parameters, the l-p-DOS results are comparable between the implemented approaches and between the two tested codes. The more evident differences arise with systems composed of atoms with different values of azimuthal quantum numbers in the valence shell, where the l-p-DOS obtained with CF-SWs diverge from the other options. This difference can be reduced by adding NGWFs in the ONETEP basis set to allow a better fitting between NGWFs and SWs. Moreover, for metallic nanoparticles of increasing size, the *d*-bands near the Fermi level, which is commonly used as a descriptor in the heterogeneous catalysis field, remain almost unaltered between different approaches, showing the robustness of the

implemented method for such studies. The availability of these methods in a linear-scaling framework such as ONETEP opens the way for analysis of the electronic structure of complex nanostructured materials.

Acknowledgments

LGV acknowledges the support of CNPq via the Science Without Borders Programme (CNPq: 206419/2014-7). JA would like to thank EPSRC for postdoctoral research funding via the CCP9 flagship project grant EP/P02209X/1. We are grateful for computational support from the UK national high performance computing service, ARCHER, for which access was obtained via the UKCP consortium and funded by EPSRC grant ref EP/P022030/1. We are grateful for access to the IRIDIS-5 supercomputer of the University of Southampton. We would like to thank Dr Victor Milman from BIOVIA/Dassault Systèmes for helpful discussions.

Conflicts of interest

There are no conflicts of interest to declare.

ORCID iDs

J Aarons https://orcid.org/0000-0002-1290-5494
L G Verga http://orcid.org/0000-0002-7453-238X
N D M Hine https://orcid.org/0000-0001-5613-3679
C-K Skylaris https://orcid.org/0000-0003-0258-3433

References

[1] Jones R O 2015 Density functional theory: its origins, rise to prominence, and future *Rev. Mod. Phys.* **87** 897–923
[2] Becke A D 2014 Perspective: fifty years of density-functional theory in chemical physics *J. Chem. Phys.* **140** 18A301
[3] Mardirossian N and Head-Gordon M 2017 Thirty years of density functional theory in computational chemistry: an overview and extensive assessment of 200 density functionals *Mol. Phys.* **115** 2315–72
[4] Hohenberg P and Kohn W 1964 Inhomogeneous electron gas *Phys. Rev.* **136** B864–71
[5] Kohn W and Sham L J 1965 Self-consistent equations including exchange and correlation effects *Phys. Rev.* **140** A1133–8
[6] Sanchez-Portal D, Artacho E and Soler J M 1995 Projection of plane-wave calculations into atomic orbitals *Solid State Commun.* **95** 685–90
[7] Sánchez-Portal D, Artacho E and Soler J M 1996 Analysis of atomic orbital basis sets from the projection of plane-wave results *J. Phys.: Condens. Matter* **8** 3859
[8] Maintz S, Deringer V L, Tchougréeff A L and Dronskowski R 2016 Lobster: a tool to extract chemical bonding from plane-wave based dft *J. Comput. Chem.* **37** 1030–5
[9] Medford A J, Vojvodic A, Hummelshøj J S, Voss J, Abild-Pedersen F, Studt F, Bligaard T, Nilsson A and Nørskov J K 2015 From the sabatier principle to a predictive theory of transition-metal heterogeneous catalysis *J. Catalysis* **328** 36–42 (special issue: the impact of haldor topse on catalysis)
[10] Jacobsen C J H, Dahl S, Clausen B S, Bahn S, Logadottir A and Nørskov J K 2001 Catalyst design by interpolation in the periodic table: bimetallic ammonia synthesis catalysts *J. Am. Chem. Soc.* **123** 8404–5
[11] Logadottir A, Rod T H, Nørskov J K, Hammer B, Dahl S and Jacobsen C J H 2001 The Brønsted–Evans–Polanyi relation and the volcano plot for ammonia synthesis over transition metal catalysts *J. Catalysis* **197** 229–31
[12] Hammer B and Nørskov J K 2000 Theoretical surface science and catalysis-calculations and concepts *Impact of Surface Science on Catalysis* (*Advances in Catalysis* vol 45) (New York: Academic) pp 71–129
[13] Nørskov J K, Abild-Pedersen F, Studt F and Bligaard T 2011 Density functional theory in surface chemistry and catalysis *Proc. Natl Acad. Sci.* **108** 937–43
[14] Vojvodic A, Nørskov J K and Abild-Pedersen F 2014 Electronic structure effects in transition metal surface chemistry *Top. Catalysis* **57** 25–32
[15] Xin H, Vojvodic A, Voss J, Nørskov J K and Abild-Pedersen F 2014 Effects of *d*-band shape on the surface reactivity of transition-metal alloys *Phys. Rev.* B **89** 115114
[16] Verga L G, Aarons J, Sarwar M, Thompsett D, Russell A E and Skylaris C-K 2016 Effect of graphene support on large pt nanoparticles *Phys. Chem. Chem. Phys.* **18** 32713–22
[17] Aarons J, Jones L, Varambhia A, MacArthur K E, Ozkaya D, Sarwar M, Skylaris C-K and Nellist P D 2017 Predicting the oxygen-binding properties of platinum nanoparticle ensembles by combining high-precision electron microscopy and density functional theory *Nano Lett.* **17** 4003–12
[18] Verga L G, Aarons J, Sarwar M, Thompsett D, Russell A E and Skylaris C-K 2018 Dft calculation of oxygen adsorption on platinum nanoparticles: coverage and size effects *Faraday Discuss.* **208** 497–522
[19] Verga L G, Russell A E and Skylaris C-K 2018 Ethanol, O, and CO adsorption on pt nanoparticles: effects of nanoparticle size and graphene support *Phys. Chem. Chem. Phys.* **20** 25918–30
[20] Hine N D M, Avraam P W, Tangney P and Haynes P D 2012 Linear-scaling density functional theory simulations of polar semiconductor nanorods *J. Phys.: Conf. Ser.* **367** 012002
[21] Clark S J, Segall M D, Pickard C J, Hasnip P J, Probert M I J, Refson K and Payne M C 2005 First principles methods using castep *Z. Kristallogr.* **220** 567–70
[22] Skylaris C-K, Haynes P D, Mostofi A A and Payne M C 2005 Introducing onetep: linear-scaling density functional simulations on parallel computers *J. Chem. Phys.* **122** 084119

[23] Skylaris C-K, Mostofi A A, Haynes P D, Pickard C J and Payne M C 2001 Accurate kinetic energy evaluation in electronic structure calculations with localized functions on real space grids *Comput. Phys. Commun.* **140** 315–22
[24] Kohn W 1996 Density functional and density matrix method scaling linearly with the number of atoms *Phys. Rev. Lett.* **76** 3168–71
[25] Ruiz-Serrano A, Hine N D M and Skylaris C-K 2012 Pulay forces from localized orbitals optimized *in situ* using a psinc basis set *J. Chem. Phys.* **136** 234101
[26] Ruiz-Serrano A and Skylaris C-K 2013 A variational method for density functional theory calculations on metallic systems with thousands of atoms *J. Chem. Phys.* **139** 054107
[27] Perdew J P, Burke K and Ernzerhof M 1996 Generalized gradient approximation made simple *Phys. Rev. Lett.* **77** 3865–8
[28] Blöchl P E 1994 Projector augmented-wave method *Phys. Rev.* B **50** 17953–79
[29] Hine N D M 2016 Linear-scaling density functional theory using the projector augmented wave method *J. Phys.: Condens. Matter* **29** 024001
[30] Vanderbilt D 1990 Soft self-consistent pseudopotentials in a generalized eigenvalue formalism *Phys. Rev.* B **41** 7892–5
[31] Garrity K F, Bennett J W, Rabe K M and Vanderbilt D 2014 Pseudopotentials for high-throughput dft calculations *Comput. Mater. Sci.* **81** 446–52
[32] Morris A J, Nicholls R J, Pickard C J and Yates J R 2014 Optados: a tool for obtaining density of states, core-level and optical spectra from electronic structure codes *Comput. Phys. Commun.* **185** 1477–85
[33] Ellaby T, Aarons J, Varambhia A, Jones L, Nellist P, Ozkaya D, Sarwar M, Thompsett D and Skylaris C-K 2018 Ideal versus real: simulated annealing of experimentally derived and geometric platinum nanoparticles *J. Phys.: Condens. Matter* **30** 155301
[34] Hine N D M, Robinson M, Haynes P D, Skylaris C-K, Payne M C and Mostofi A A 2011 Accurate ionic forces and geometry optimization in linear-scaling density-functional theory with local orbitals *Phys. Rev.* B **83** 195102